Petroleum Science 23 (2026) 4280–4295

Contents lists available at ScienceDirect

Petroleum Science

journal homepage: www.keaipublishing.com/en/journals/petroleum-science

Original Paper

Energy-driven damage constitutive model of thermal insulation materials for deep rock in-situ temperature-preserved coring

Zi-Jie Wei [a,b], Zhi-Qiang He [a,b,*], Ling Chen [b,c], Bo Yu [b,c], Jian-Ping Yang [b,d], Hai-Shu Bai [b,c], He-Ping Xie [a,b,e]

[a] State Key Laboratory of Hydraulics and Mountain River Engineering, College of Water Resource and Hydropower, Sichuan University, Chengdu, 610065, Sichuan, China
[b] State Key Laboratory of Intelligent Construction and Healthy Operation and Maintenance of Deep Underground Engineering, Sichuan University, Chengdu, 610065, Sichuan, China
[c] College of Mechanical Engineering, Sichuan University, Chengdu, 610065, Sichuan, China
[d] College of Polymer Science and Engineering, Sichuan University, Chengdu, 610065, Sichuan, China
[e] Guangdong Provincial Key Laboratory of Deep Earth Sciences and Geothermal Energy Exploitation and Utilization, Institute of Deep Earth Sciences and Green Energy, College of Civil and Transportation Engineering, Shenzhen University, Shenzhen, 518060, Guangdong, China

ARTICLE INFO

Article history:
Received 26 June 2025
Received in revised form
4 February 2026
Accepted 13 April 2026
Available online 21 April 2026

Edited by Xi Zhang

Keywords:
In-situ temperature-preserved coring (ITP-Coring)
High-temperature and high-pressure (HTHP) environments
Hollow glass microsphere/epoxy thermal insulation materials (HGM/EP materials)
Energy evolution behaviour
Statistical damage constitutive model

ABSTRACT

Accurate evaluation of deep oil and gas reservoirs critically depends on key properties such as rock porosity and permeability, which are significantly affected by high-temperature conditions in deep formations. In-situ temperature-preserved coring (ITP-Coring) is a prerequisite for reliable assessment of deep rock properties, with thermal insulation materials serving as its key component. This study investigates the performance variation law and damage evolution characteristics of thermal insulation materials under high-temperature and high-pressure conditions. The findings show that at elevated temperatures, the material compressive strength decreases to one-fourth to one-fifth of its value at room temperature, while the peak compressive strain increases by two to three times. Furthermore, the energy evolution and damage characteristics of the hollow glass microsphere/epoxy thermal insulation materials (HGM/EP materials) during uniaxial compression were analyzed, and an energy-driven statistical damage constitutive model was established, which effectively predicts the stress–strain behaviour of HGM/EP materials after temperature-pressure preconditioning. The correlation between initial damage d and pretreatment temperature and pressure was also examined. It was found that when the pretreatment pressure is below 100 MPa, the threshold temperature at which initial damage sharply increases is 100 °C. An initial damage evolution model considering temperature and pressure effects was established, and the relationship between damage rate, temperature, pressure and initial damage was analyzed. The research results provide a theoretical basis for the application of thermal insulation materials under extreme conditions in deep ITP-Coring operations.

1. Introduction

As the Earth's resources continue to be exploited, the gradual depletion of shallow subsurface deposits has driven resource exploration and development toward greater depths (Xie et al., 2015, 2019, 2023). In the context of plentiful oil and gas resources, China has initiated two ultra-deep scientific exploration wells: the Deep Earth TK1 Well and the Deep Earth CK1 Well. Notably, the TK1 Well surpassed the 10,000 m mark on March 4, 2024, achieving a final drilled depth of 10,910 m. Concurrently, the CK1 Well is currently being drilled toward its target depth of 10,520 m (Sun et al., 2024). Deep oil and gas resources are in high-temperature environments, with a geothermal gradient of up 30–50 °C/km (Liu et al., 2016). High temperatures can markedly affect key properties such as rock permeability and porosity, which are critical for accurate assessment of deep subsurface oil and gas reserves (Chandra et al., 2021; Lin et al., 2023; Saif et al., 2017). Therefore, accurate evaluation of reservoir rock characteristics is a

* Corresponding author.
E-mail address: hzqscu@scu.edu.cn (Z.-Q. He).
Peer review under the responsibility of China University of Petroleum (Beijing).

https://doi.org/10.1016/j.petsci.2026.04.018

core component of deep hydrocarbon resource exploration and exploitation. However, core samples obtained by conventional coring methods cannot maintain their in-situ physical and mechanical characteristics. As a result, the rock properties derived from such core samples are often inadequate for accurately assessing the in-situ conditions of deep resources (Xie et al., 2020). Therefore, developing in-situ temperature-preserved coring (ITP-Coring) technology is imperative to acquire cores that retain their original temperature conditions (Xie et al., 2021, 2023).

An important component of the deep ITP-Coring technology is thermal insulation materials. However, deep high-temperature and high-pressure (HTHP) environments make it difficult for existing thermal insulation materials to be directly applied. Composite materials made from hollow glass microspheres and epoxy resin exhibit properties such as high-pressure and high-temperature resistance and low thermal conductivity, making them ideal thermal insulation materials for ITP-coring in deep reservoirs (He et al., 2020, 2022; Yang et al., 2022). However, during the application of hollow glass microsphere/epoxy thermal insulation materials (HGM/EP materials) in extreme HTHP environments, damage inevitably occurs, which can affect their physical and mechanical properties (He et al., 2024a). Therefore, to ensure that thermal insulation materials perform effectively during the ITP-Coring process, there is an urgent need to conduct research on the damage evolution and property changes of HGM/EP materials under HTHP conditions.

Researchers have extensively studied the properties of particle-reinforced epoxy resin matrix composites under conventional conditions (Wu et al., 2021; Cao et al., 2023; Bao et al., 2020). Meanwhile, such high-performance materials have been widely applied across multiple sectors, including oil and gas (Huang and Li, 2015; Chen et al., 2021; Yang et al., 2022; Sue et al., 2022), aerospace (Zhang et al., 2016; Porfiri and Gupta, 2009; Doddamani, 2019; Tong et al., 2021; Abedin et al., 2022), and marine engineering (Garcia et al., 2018; Shahapurkar et al., 2018; Pei et al., 2025; Li et al., 2024). This growing adoption has driven increased research efforts to characterize material behaviors under diverse temperature-pressure conditions. For instance, Schumacher et al. (2024) investigated the correlation between filler volume fraction and the material compressive strength/energy absorption efficiency. Phan et al. (2013) analyzed the long-term mechanical performance of deep-sea oil pipeline insulation materials through creep experiments. Zhang et al. (2022) systematically studied the strain rate effects and energy absorption capacity of aero-engine materials at temperatures from 25 °C to 150 °C. Wang and Cui (2023) developed a multiscale hydro-mechanical coupling model by analyzing the water absorption characteristics of buoyancy materials in low-temperature, high-pressure deep-sea environments. Additionally, Liu (2019) and Zhai et al. (2020) separately examined the pressure resistance of HGM-reinforced composites under 60 MPa hydrostatic pressure, investigating strain patterns and yield strength characteristics for materials with varying microsphere strengths or volume fractions. He et al. (2022) demonstrated that high pressure predominantly affects compressive strength while having a negligible effect on tensile strength. Zhai et al. (2022, 2023) further investigated the compressive mechanical properties of deep-sea buoyancy materials under diverse temperature-pressure states and developed a failure criterion accounting for tension-compression asymmetry. Wei et al. (2025) employed dynamic thermomechanical analysis to explore the evolution of interfacial performance between the matrix and fillers in composites with different filler strengths and volume fractions after HTHP pretreatment.

In summary, many valuable findings have been obtained from studies on the properties of particle-reinforced epoxy resin matrix composites under different temperature and pressure conditions. However, relatively few studies have been conducted to characterize the damage evolution of such materials in HTHP environments. Therefore, based on previous studies (He et al., 2024a, 2024b; Wei et al., 2023, 2024), this paper further investigates the energy evolution characteristics of HGM/EP materials after exposure to HTHP environments from a thermodynamic perspective. Building upon this, a statistical damage constitutive model for thermal insulation materials is developed. By introducing a dissipative energy weighting factor and a corresponding coefficient, this model effectively captures the changes in the mechanical properties of thermal insulation materials after different temperature and pressure pretreatments. The model reproduces the complete stress–strain curve, including the elastic, yielding, and material failure stages. Additionally, this study further analyzes the initial damage formed in thermal insulation materials after treatment under different temperature and pressure conditions. This study establishes a coupled temperature-pressure evolution model for the initial damage in HGM/EP materials after temperature-pressure pretreatment. Furthermore, it explores the relationship between the material damage rate and the temperature, pressure, and initial damage. The results provide the theoretical basis for the application of HGM/EP materials in deep ITP-Coring technology.

2. Preparation of thermal insulation materials and experimental methods

2.1. Material preparation methods

Based on previous research, this study used K46 HGMs (3 M science, Saint Paul, United States) as the filler, with volume fractions of 40% and 50%. The matrix formulation incorporated E-51 epoxy resin (Nantong Xingchen Synthetic Materials, China), and utilized 2-ethyl-4-methylimidazole curing agent (Macklin Biochemical, China). The prepared cylindrical compression specimens had dimensions of ϕ12 mm × 20 mm. The specific preparation method for the HGM/EP material specimens can be referenced from previous studies (Wei et al., 2025).

2.2. HTHP pretreatment method

In this work, the HGM/EP materials were pretreated with controlled temperature and pressure environments by means of the Deep In-Situ Environmental Simulator (State Key Laboratory of Intelligent Construction and Health Maintenance for Deep Underground Engineering, Sichuan University), a specialized apparatus capable of replicating extreme conditions reaching 160 °C thermal load and 200 MPa confining pressure. The device maintains a temperature control accuracy of ±3 °C and a pressure control accuracy of ±2 MPa, with a heating rate of 1.5 to 1.8 °C/min. Pressure control within the vessel is achieved using a pneumatic ultra-high-pressure pump with pure water as the working medium (Shi et al., 2025). Four gradients were set for each variable: temperature (25, 50, 100, 150 °C) and pressure (0, 50, 100, 140 MPa). This resulted in 16 distinct temperature-pressure coupled treatment conditions. Specific pretreatment methods are described in previous studies (Wei et al., 2025).

Based on different temperature and pressure pretreatment conditions, and considering the volume fraction of K46 HGMs, the HGM/EP materials were labeled accordingly. For example, K46-f40-H140-T150 refers to an HGM/EP material sample with 40%

K46 microsphere volume fraction that was treated at 140 MPa and 150 °C.

2.3. Testing method for physical and mechanical properties

The mass of the HGM/EP materials before and after temperature-pressure pretreatment is measured as m_1 and m_2, respectively. The mass change is calculated using the following Eq. (1):

$$\omega = \frac{m_2 - m_1}{m_1} \times 100\% \quad (1)$$

Quantification of heat transfer characteristics in the HGM/EP materials was performed via the TPS2500S hot disk system. Mechanical properties evaluation employed an Instron electromechanical testing platform configured for uniaxial compression characterization. During both the thermal conductivity and mechanical property tests, the materials were maintained at their corresponding pretreatment temperatures for measurement. Detailed testing procedures were described in previous studies (Wei et al., 2025).

3. Analysis of physical and mechanical properties of thermal insulation materials

3.1. Analysis of physical properties

Fig. 1 delineates the interdependent variations in water absorption rate and heat transfer coefficients after different temperature-pressure pretreatment. The trends in the changes in thermal conductivity are highly consistent with those of the water absorption rate. When the pressure is up to 50 MPa, the water absorption rate of the material increases with the rising pretreatment temperature, and the rate of increase becomes more significant. Correspondingly, the thermal conductivity of the material also increases. At pressures not exceeding 100 MPa, the temperature threshold of a remarkable rise in water absorption rate is approximately 100 °C. However, when the pressure reaches 140 MPa, the temperature threshold of a noticeable rise in water absorption drops to 50 °C, with the threshold for the K46-f50 material being even lower.

It can be observed that pressure is the dominant factor in material water absorption. Under high hydrostatic pressure, fluid penetration is facilitated, damaging the interface between the microspheres and the substrate. This damage results in the cracking of the microsphere. The infiltrated water, an efficient thermal conductor, significantly increases the thermal conductivity of the material. Elevated temperature also plays a key role by increasing the molecular chain mobility, thereby further promoting heat transfer.

3.2. Analysis of mechanical properties

As shown in Fig. 2, the variations in elastic modulus E, compressive strength σ_c, and the corresponding compressive strain at the peak point (hereafter referred to as peak point compressive strain ε_c) are presented as functions of pretreatment temperature under different hydrostatic pressures. With increasing temperature, the compressive strength σ_c and elastic modulus E decrease consistently. Furthermore, the extent of reduction in compressive strength with temperature exhibits a clear dependence on the pretreatment pressure.

At a pretreatment pressure is 0 MPa, the rate of decrease in compressive strength with temperature follows a two-stage pattern: slow initially, then fast. When the pretreatment pressure is increased but does not exceed 100 MPa, the decrease in compressive strength with temperature exhibits an approximately linear trend. The rate of decrease is similar to the average rate of the two-stage decline observed under atmospheric pressure. While the hydrostatic pressure rises to 140 MPa, the rate of decrease again shows a two-stage pattern, but with the sequence reversed: fast initially, then slow. The transition temperature for this rate change is consistent with that under atmospheric pressure treatment, occurring at approximately 100 °C. In summary, compressive strength decreases with increasing temperature at all pretreatment pressures, and higher pressure accelerates this reduction.

The peak point compressive strain ε_c exhibits a distinct temperature threshold. Below this threshold, εc remains nearly constant, whereas it increases rapidly once the temperature is exceeded. At pressures $\leq$100 MPa, this threshold is approximately 100 °C. When the pressure reaches 140 MPa, the threshold drops to 50 °C or lower. Furthermore, the higher the pressure, the increase in compressive strain at the peak point. This behavior is consistent with the trend observed for water absorption, indicating that water infiltrated under high pressure facilitates plastic deformation. Concurrently, elevated temperature enhances the molecular chain mobility of the HGM/EP composite, promoting a transition

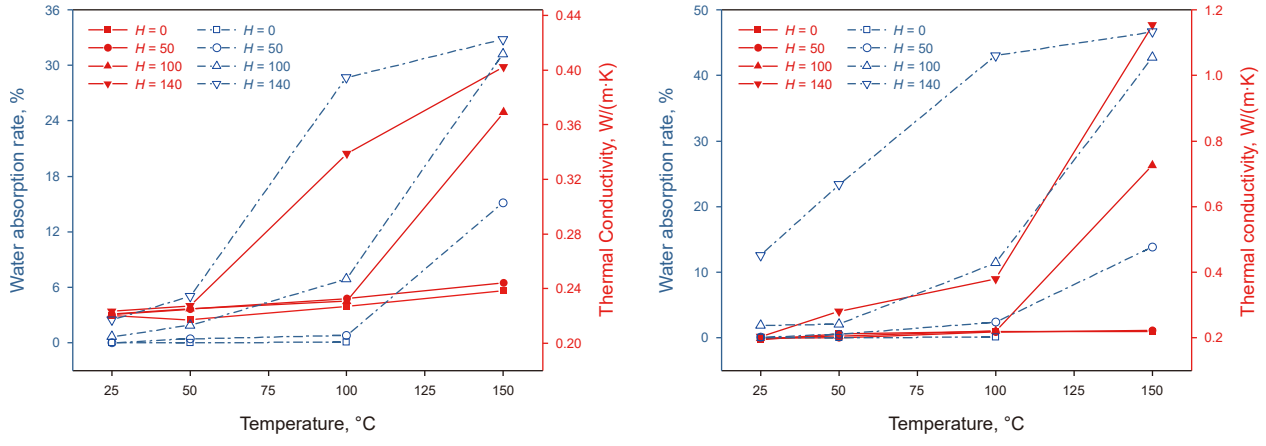

Fig. 1. Variation curves of physical properties of HGM/EP materials.

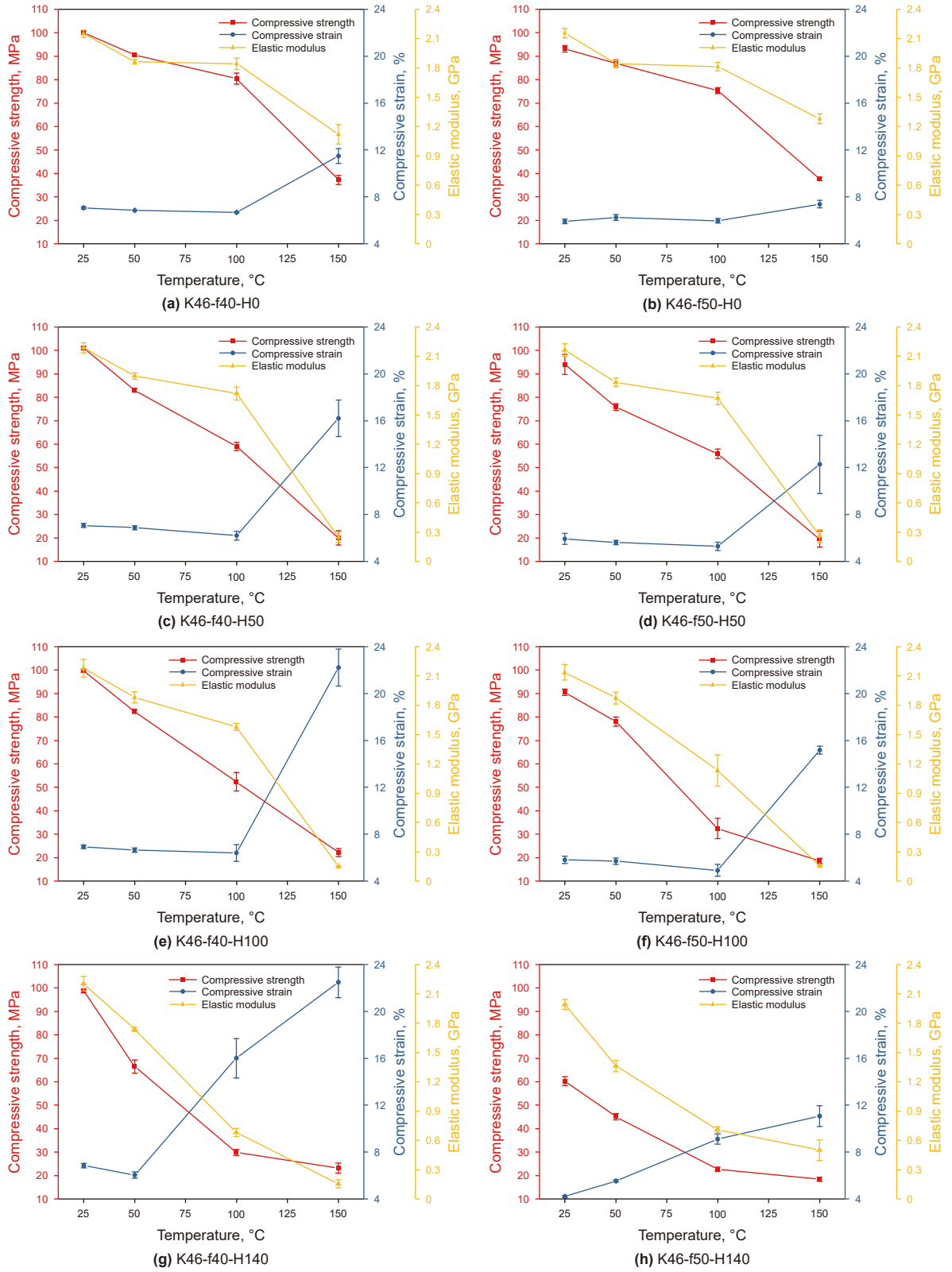

Fig. 2. Change curves of mechanical properties of HGM/EP materials under different pressures.

toward viscoelastic behavior, which further contributes to the plastic deformation.

Additionally, the peak point compressive strain ε_c and compressive strength σ_c of the K46-f50 material are both lower than those of the K46-f40 material. This observation supports the hypothesis that a higher HGM volume fraction results in more brittle material behavior. Excessively high HGM volume fractions reduce the material compressive strength

because the HGMs are difficult to fully impregnate with the matrix, leading to poor interfaces. These inferior interfaces reduce the internal microstructure, resulting in lower overall compressive strength.

Based on the preceding analysis, HGM/EP materials subjected to HTHP pretreatment generally exhibit three typical stress–strain curves, as shown in Fig. 3. For materials treated at low temperatures (below 50 °C), the stress–strain curve exhibits a brittle failure characteristic with a relatively high compressive strength, as shown in typical curve I in Fig. 3. The curve is primarily dominated by elastic deformation, with a very short yield stage, and culminates in abrupt failure due to the sudden release of stored elastic energy.

For materials treated at high temperatures (150 °C), the stress–strain response in typical curve III in Fig. 3 is characterized by distinct plastic failure. The compressive strain at failure is substantially larger—typically two to three times greater than that of low-temperature-treated materials. The initial elastic deformation stage is brief, followed by a pronounced yield and plateau stage dominated by plastic deformation. Correspondingly, the compressive strength is markedly lower, reduced to approximately one-quarter to one-fifth of the strength observed in low-temperature-treated materials.

The stress–strain curve of materials treated at intermediate temperatures (100 °C) exhibits intermediate characteristics between the two patterns described above, as represented by typical curve II in Fig. 3. Both elastic and plastic deformation regimes are well-defined. With increasing pretreatment temperature within this range, compressive strength decreases progressively while the peak compressive strain increases accordingly.

The continuous progression among these three characteristic curves reflects the transition in the mechanical behavior of HGM/EP composites across different temperature conditions. Pretreatment pressure primarily influences the stress–strain response by promoting a shift from brittle to plastic failure modes. Specifically, with increasing pretreatment pressure, the temperature required for the transition from typical curve I to typical curve II behavior is lowered, and the transition occurs over a narrower temperature range, accompanied by a concurrent increase in the peak compressive strain.

3.3. Energy evolution law

To further analyze the evolution of compressive damage in HGM/EP materials, the energy input, accumulation, dissipation and release throughout the complete compression failure process were considered. These can be categorized into three types of energy: elastic energy, dissipated energy, and total input energy. The relationship among these three types of energy is expressed in Eq. (2) (Xie et al., 2005).

$$U = U^{d} + U^{e} \tag{2}$$

where U represents the input energy density generated by external work, kJ/m^3; U^e is the elastic energy density stored in the HGM/EP materials, kJ/m^3; and U^d is the dissipated energy density during the deformation and failure process of the HGM/EP materials, kJ/m^3. The calculation methods for these three energy densities are given in Eqs. (3)–(5) (Xie et al., 2005).

$$U^{e} = \frac{\sigma_i^2}{2E} \tag{3}$$

$$U = \int_0^{\varepsilon_i} \sigma_i \mathrm{d}\varepsilon \tag{4}$$

$$U^{d} = U - U^{e} \tag{5}$$

where E denotes the unloading elastic modulus, MPa. In calculating the elastic strain energy density, the initial elastic modulus E_0 is often used to approximate E.

Based on the above equations, the variation curves of compressive energy of HGM/EP materials with temperature and compressive strain under different pretreatment pressures were plotted, as shown in Fig. 4.

When the hydrostatic pressure is 0 MPa and the temperature does not exceed 100 °C, the energy evolution of the HGM/EP materials is dominated by elastic energy, while the dissipated energy rises slowly. It is because the epoxy resin matrix remains in the glassy state, exhibiting a high elastic modulus and strong energy storage capacity. However, at 150 °C, the dissipated energy density increases sharply at a relatively low compressive strain and

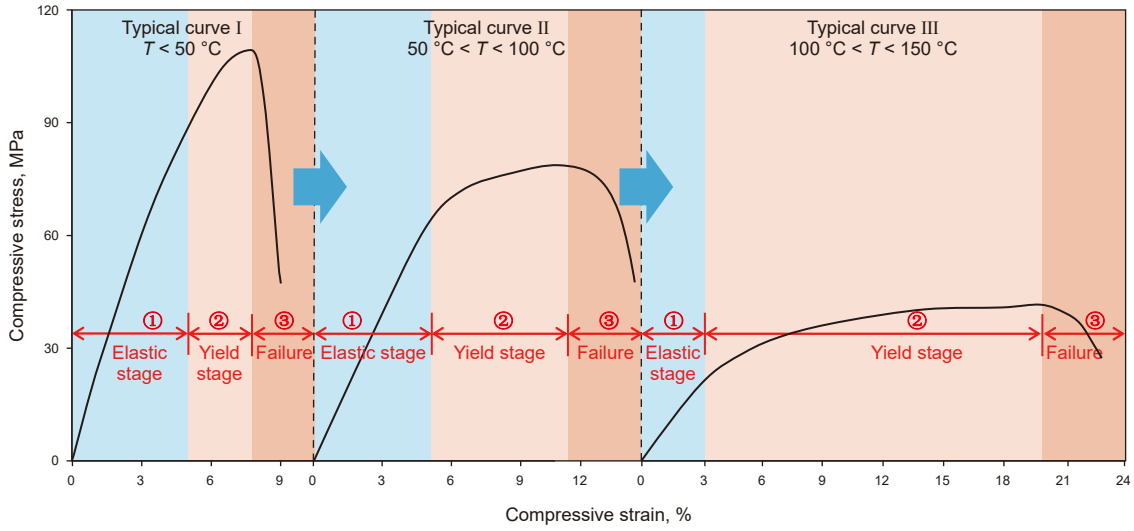

Fig. 3. Typical stress–strain curves of HGM/EP materials at different temperature and pressure situations.

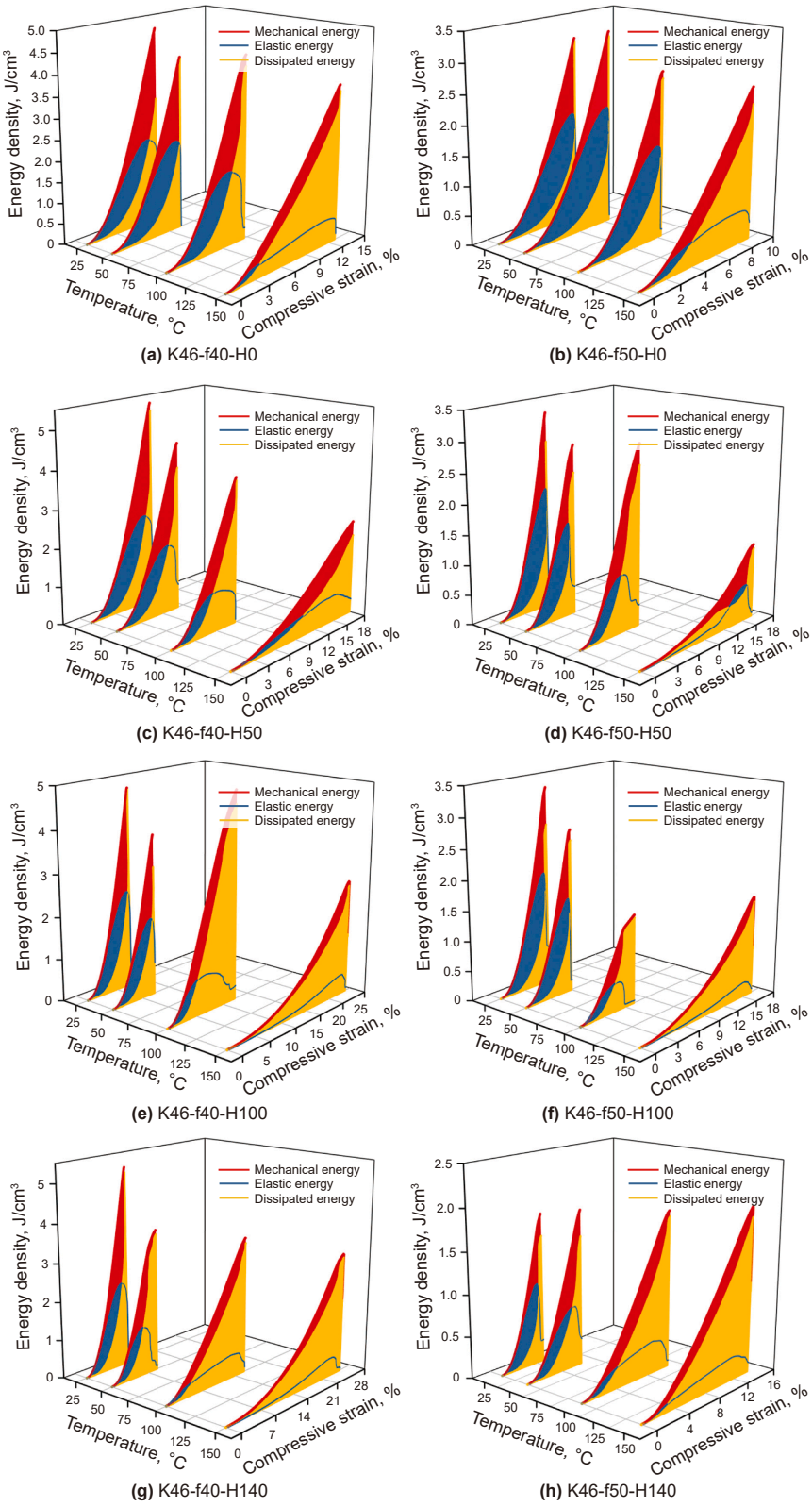

Fig. 4. Energy evolution of HGM/EP materials under different temperature and pressure conditions.

surpasses the elastic energy density. Concurrently, the rate of increase in elastic energy density decreases significantly. Notably, even when the dissipated energy density becomes substantially higher than the elastic energy density, the HGM/EP materials have not yet reached their peak compressive strength. This pre-peak energy distribution contrasts sharply with behavior at other temperatures, where the dissipated energy density remains lower than the elastic energy density prior to failure.

This phenomenon is attributed to the ambient temperature is close to the glass transition temperature of the HGM/EP material (163.7–172 °C) (Wei et al., 2025), which intensifies the motion of molecular chain segments. This enhanced molecular mobility promotes viscous flow or localized plastic deformation, resulting in additional energy dissipation. Macroscopically, this results in a sharp decline in both compressive strength and elastic modulus, along with an increase in pre-peak strain. These findings indicate a transition in the damage mode of HGM/EP materials at 150 °C.

Under atmospheric pressure, while the temperature exceeds 100 °C, the damage mode of HGM/EP materials transitions from elasticity-dominated energy storage regime to a dissipation-dominated regime characterized by matrix plastic deformation, interfacial damage, and microsphere failure.

At hydrostatic pressures of 50 MPa or 100 MPa, the evolution of energy density in the HGM/EP materials similarly shifts from elasticity-dominated storage to damage-induced dissipation, with 100 °C acting as a threshold temperature. As the temperature increases, material stiffness decreases continuously, and the peak compressive strain at 150 °C increases significantly, reaching two to three times the values observed below 100 °C. High-temperature pretreatment intensifies the motion of molecular chain segments, while high-pressure pretreatment promotes water absorption in the materials. During uniaxial compression, HGM/EP materials undergo viscoelastic deformation, which reduces the probability of interfacial debonding and localized collapse of microspheres, thereby delaying the onset of dissipation mechanisms. This phenomenon can still be observed in the variation curves under the H140-T150 condition. Macroscopically, this condition is characterized by a substantial increase in compressive strain and a pronounced reduction in elastic modulus. The compressive strain at peak strength reaches 16%–24%, and the elastic modulus is approximately 0.15 GPa.

Notably, the compressive-shear failure characteristics of HGM/EP materials transition from a multiple-fracture-surface mode to a single-fracture-surface mode under varying temperature and pressure conditions. When the pretreatment pressure is 0 MPa, the materials pretreated at different temperatures exhibit the multiple-fracture-surface mode. In contrast, at a pretreatment pressure of 140 MPa, a single-fracture-surface mode was observed under all temperature conditions. For intermediate pretreatment conditions, the failure mode progressively transitions from multiple surfaces to a single surface with increasing temperature and pressure (He et al., 2024a), indicating a strong correlation between the failure mechanism and the pretreatment temperature-pressure parameters. The initial damage zones formed during temperature-pressure pretreatment serve as preferential pathways for damage propagation during subsequent compression, as shown in Fig. 5. Consequently, materials pretreated under HTHP conditions exhibit the single-fracture-surface mode.

In summary, the failure mechanisms of HGM/EP materials pretreated under HTHP conditions are influenced by multiple factors, including phase and structural changes of the matrix as well as damage to microspheres and interfaces. At different temperatures, as the pretreatment pressure increases from 0 MPa to 140 MPa, the peak values and growth rates of mechanical energy density and elastic energy density gradually decline. Additionally, the critical strain at which dissipated energy density exceeds

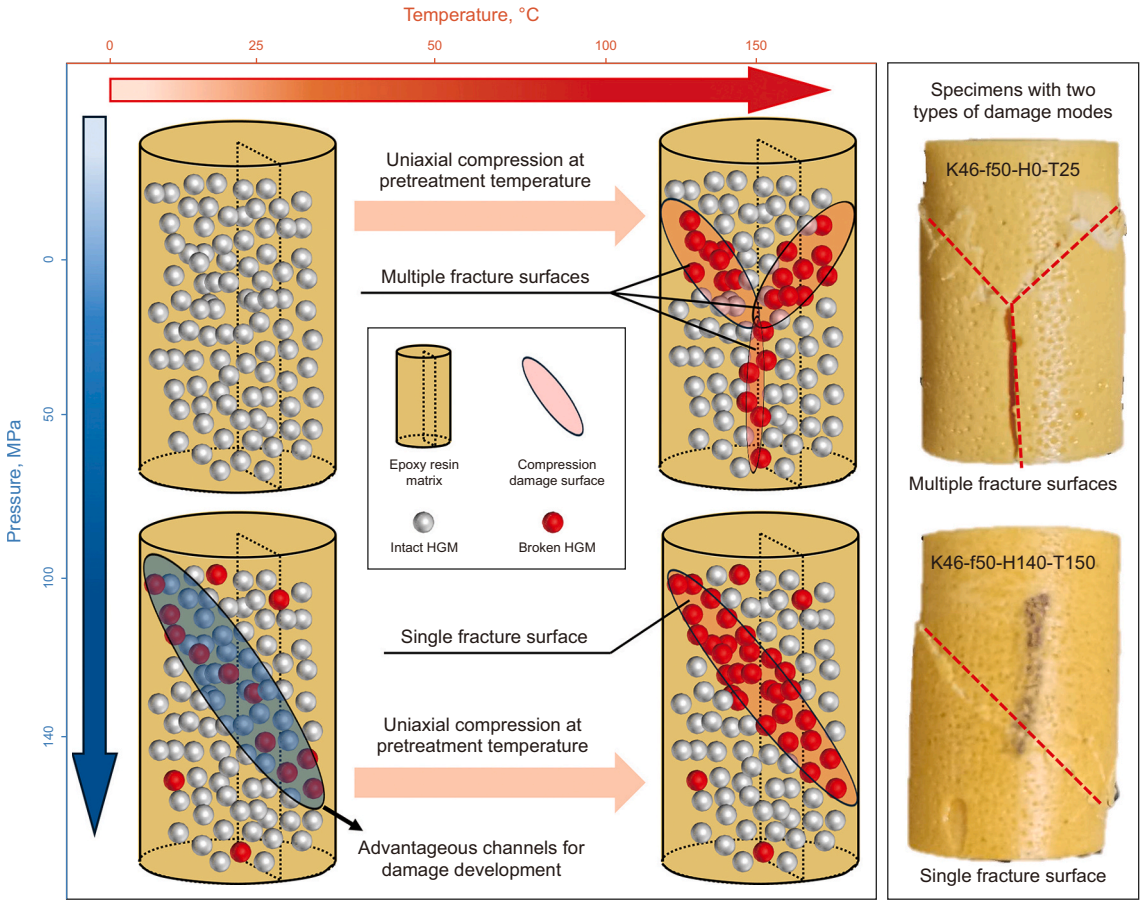

Fig. 5. Schematic diagram of failure modes of HGM/EP materials under different temperature and pressure pretreatment conditions.

elastic energy density also decreases. This is attributed to the enhanced water absorption of the matrix and the accelerated accumulation of internal structural damage under higher pretreatment pressures. In the low-pressure range (0–50 MPa), the dominant energy accumulation mechanism transitions from elastic energy storage governed by the matrix to energy dissipation dominated by damage to multiple constituent phases. Due to the phase transition occurring in the epoxy resin matrix at elevated temperatures near the glass transition temperature, material deformation is primarily dominated by plastic deformation of the matrix, characterized by a gradual increase in dissipated energy.

4. Statistical damage constitutive model of thermal insulation materials based on the principle of energy dissipation and release

To further analyze the damage induced in HGM/EP materials by HTHP pretreatment, the dissipated energy is employed as a damage metric. A statistical damage constitutive model is developed to investigate the damage evolution behavior of HGM/EP materials after undergoing HTHP pretreatment.

4.1. Establishment of the statistical damage constitutive model

Based on the Lemaitre strain equivalence principle (Lemaitre, 1984), the constitutive relationship of the damaged material can be obtained as shown in Eq. (6):

$$\sigma = \sigma^*(1-D) = E\varepsilon(1-D) \tag{6}$$

where σ and σ^* are nominal and effective stresses, respectively, and D is the damage variable.

The HGM/EP thermal insulation materials are composed of an epoxy resin matrix, hollow glass microspheres as fillers, and the interface formed between them. These materials can be viewed as being made up of numerous representative volume elements (RVEs), each containing the matrix, microspheres, and interface phase. The RVEs are sufficiently small on the macroscopic scale and large enough on the microscopic scale so that the mechanical property changes of the RVEs can be regarded as equivalent to those of the bulk HGM/EP material. The damage of HGM/EP materials during loading is treated as a sequential process and it is assumed that:

(1) The material is macroscopically isotropic.
(2) Each RVE has only two possible states—either intact or failed—characterized by a binary (0–1) distribution.
(3) RVEs obey Hooke law before failure and lose their load-bearing capacity after failure.
(4) The RVEs are randomly distributed within the material, and the resulting damage is also randomly distributed.

Thus, the mechanical behaviour of the RVEs can be depicted statistically. Assuming the ratio between the dissipated energy density U^{d} and the dissipated energy density corresponding to the peak stress $U_{\mathrm{p}}^{\mathrm{d}}$ represents the RVE strength χ (Eq. (7)), it is assumed to follow the Weibull distribution (Eq. (8)).

$$\chi = \frac{U^{\mathrm{d}}}{U_{\mathrm{p}}^{\mathrm{d}}} \tag{7}$$

$$P[\chi] = \frac{k}{m}\left(\frac{\chi}{m}\right)^{k-1}\exp\left[-\left(\frac{\chi}{m}\right)^{k}\right] \tag{8}$$

where $P[\chi]$ is the function of probability density of the Weibull distribution, m is the scale parameter, and k is the shape parameter of the distribution.

During the uniaxial compression process, as the compressive strain increases, HGM/EP materials continuously accumulate damage, which is reflected by the progressive increase in dissipated energy. The number of damaged RVEs in the material, denoted as N_D, can be expressed as:

$$\begin{aligned} N_D &= N\int P[\chi]\mathrm{d}(\chi) = N\int \frac{k}{m}\left(\frac{\chi}{m}\right)^{k-1}\exp\left[-\left(\frac{\chi}{m}\right)^{k}\right]\mathrm{d}(\chi) \\ &= N\left\{1-\exp\left[-\left(\frac{\chi}{m}\right)^{k}\right]\right\} \end{aligned} \tag{9}$$

where N_D is the number of damaged RVEs, and N is the number of total RVEs.

The ratio of the number of damaged RVEs to the total number of RVEs in the HGM/EP material is the damage variable D, which can be expressed as:

$$D = \frac{N_D}{N} \tag{10}$$

Substituting Eq. (9) into Eq. (10) gives the damage factor D that describes the damage characteristics of the HGM/EP material (Xiao et al., 2023):

$$D = 1-\exp\left[-\left(\frac{\chi}{m}\right)^{k}\right] \tag{11}$$

Substituting Eq. (11) into Eq. (6) yields the statistical damage constitutive model for the HGM/EP material:

$$\sigma = E\varepsilon\exp\left[-\left(\frac{\chi}{m}\right)^{k}\right] \tag{12}$$

4.2. Determination of distribution parameters for the statistical damage constitutive model

The statistical damage constitutive model has two parameters, m and k. Current methods for determining these parameters include the linear fitting method (Xiao et al., 2023), inverse analysis method (Deng and Cu, 2011), and peak point method (Xu and Karakus, 2018). The peak point method defines RVE strength through energy density, enabling parameters m and k to effectively capture the transition from elastic to plastic failure with clear physical significance. In contrast, the linear fitting method relies on data fitting of the full stress–strain curve and is susceptible to experimental noise; the inverse analysis method requires complex iterations and incurs high computational costs. In comparison, the peak point method offers clear physical interpretation and computational simplicity. Therefore, this paper employs the peak point method to resolve for the parameters m and k in the statistical damage constitutive model, as follows:

$$\sigma(\varepsilon)|_{\varepsilon=\varepsilon_c} = \sigma_c \tag{13}$$

$$\left.\frac{\mathrm{d}\sigma}{\mathrm{d}\varepsilon}\right|_{\varepsilon=\varepsilon_c} = 0 \tag{14}$$

σ_c and ε_c represent the peak compressive stress and the corresponding strain of the HGM/EP material during uniaxial compression, respectively.

By differentiating Eq. (12), we obtain:

$$\frac{\mathrm{d}\sigma}{\mathrm{d}\varepsilon}=E\exp\left[-\left(\frac{\chi}{m}\right)^{k}\right]\left[1-\frac{\varepsilon k}{m}\left(\frac{\chi}{m}\right)^{k-1}\left(\frac{\mathrm{d}\chi}{\mathrm{d}\varepsilon}\right)\right] \tag{15}$$

Substituting Eq. (12) into Eq. (13) gives:

$$\sigma_{\mathrm{c}}=E\varepsilon_{\mathrm{c}}\exp\left[-\left(\frac{\chi_{\mathrm{c}}}{m}\right)^{k}\right] \tag{16}$$

Since Eq. (16) is not equal to zero, substituting Eq. (15) into Eq. (14) simplifies to:

$$1-\frac{\varepsilon_{\mathrm{c}}k}{m}\left(\frac{\chi_{\mathrm{c}}}{m}\right)^{k-1}\left(\frac{\mathrm{d}\chi}{\mathrm{d}\varepsilon}\right)|_{\varepsilon=\varepsilon_{\mathrm{c}}}=0 \tag{17}$$

After rearranging terms, Eq. (17) becomes:

$$\frac{\varepsilon_{\mathrm{c}}k}{m}\left(\frac{\chi_{\mathrm{c}}}{m}\right)^{k-1}\left(\frac{\mathrm{d}\chi}{\mathrm{d}\varepsilon}\right)|_{\varepsilon=\varepsilon_{\mathrm{c}}}=1 \tag{18}$$

where, $\frac{\mathrm{d}\chi}{\mathrm{d}\varepsilon}=\frac{\sigma-E\varepsilon}{U_{\mathrm{p}}^{\mathrm{d}}}=\frac{\sigma-(\sigma/E)*(\mathrm{d}\sigma/\mathrm{d}\varepsilon)}{U_{\mathrm{p}}^{\mathrm{d}}}$, thus Eq. (18) can be simplified as:

$$\left(\frac{\chi_{\mathrm{c}}}{m}\right)^{k}=\frac{1}{2k} \tag{19}$$

$$\left(\frac{\chi_{\mathrm{c}}}{m}\right)^{k}=\frac{U_{\mathrm{c}}^{\mathrm{d}}}{k\varepsilon_{\mathrm{c}}\sigma_{\mathrm{c}}} \tag{20}$$

Substituting Eq. (19) into Eq. (16) gives k_1 and m_1:

$$k_1=\frac{1}{2\ln(E\varepsilon_{\mathrm{c}}/\sigma_{\mathrm{c}})} \tag{21}$$

$$m_1=\frac{\chi_{\mathrm{c}}}{\sqrt[k_1]{\ln(E\varepsilon_{\mathrm{c}}/\sigma_{\mathrm{c}})}} \tag{22}$$

Substituting Eq. (20) into Eq. (16) gives k_2 and m_2:

$$k_2=\frac{U_{\mathrm{c}}^{\mathrm{d}}}{\varepsilon_{\mathrm{c}}\sigma_{\mathrm{c}}\ln(E\varepsilon_{\mathrm{c}}/\sigma_{\mathrm{c}})} \tag{23}$$

$$m_2=\frac{\chi_{\mathrm{c}}}{\sqrt[k_2]{U_{\mathrm{c}}^{\mathrm{d}}/k_2\varepsilon_{\mathrm{c}}\sigma_{\mathrm{c}}}}=\frac{\chi_{\mathrm{c}}}{\sqrt[k_2]{\ln(E\varepsilon_{\mathrm{c}}/\sigma_{\mathrm{c}})}} \tag{24}$$

by comparing Eq. (21) to Eq. (24), it can be observed that k_1 and k_2 have the same expression as m_1 and m_2. Let the dissipated energy weight factor be $\eta=2U_{\mathrm{c}}^{\mathrm{d}}/\varepsilon_{\mathrm{c}}\sigma_{\mathrm{c}}$, which represents the relative proportion of the dissipated energy density to the input energy density of the HGM/EP material. Let the stiffness degradation factor be $\gamma=\ln(E\varepsilon_{\mathrm{c}}/\sigma_{\mathrm{c}})$, which can be used to determine the relative degradation of the material initial elastic modulus at the peak point. Then, Eq. (21) to Eq. (24) becomes:

$$k_1=\frac{1}{2\gamma},m_1=\frac{\chi_{\mathrm{c}}}{\sqrt[k_1]{\gamma}} \tag{25}$$

$$k_2=\frac{\eta}{2\gamma},m_2=\frac{\chi_{\mathrm{c}}}{\sqrt[k_2]{\gamma}} \tag{26}$$

where, Eq. (25) directly reflects the degree of material stiffness degradation due to matrix fracture, microsphere fragmentation, and other component damage. Eq. (26) further reflects the contribution of fragmented microspheres or matrix plastic deformation to the material damage during compression, incorporating the dissipated energy ratio (η). The contributions of these two mechanisms to damage accumulation vary at different temperature and pressure situations. To accurately represent the mechanical properties of HGM/EP materials at varying temperature and pressure conditions, dynamic weighting factors α and β are introduced to adjust the contributions of these two mechanisms, as follows:

$$k=\alpha k_1+\beta k_2=\frac{1}{2\gamma}(\alpha+\beta\eta) \tag{27}$$

$$m=\alpha m_1+\beta m_2=\frac{\alpha\chi_{\mathrm{c}}}{\sqrt[k_1]{\gamma}}+\frac{\beta\chi_{\mathrm{c}}}{\sqrt[k_2]{\gamma}}=\left(\frac{\alpha}{\sqrt[k_1]{\gamma}}+\frac{\beta}{\sqrt[k_2]{\gamma}}\right)\chi_{\mathrm{c}} \tag{28}$$

where $\alpha+\beta=1$, by substituting data from partial uniaxial compression tests under different temperature and pressure conditions, the distribution parameters and corresponding α and β can be obtained. Substituting Eqs. (27) and (28) into Eq. (12) yields the statistical damage constitutive model for HGM/EP materials:

$$\sigma=E\varepsilon\exp\left[-\left(\chi\Big/\left(\frac{\alpha}{\sqrt[k_1]{\gamma}}+\frac{\beta}{\sqrt[k_2]{\gamma}}\right)\chi_{\mathrm{c}}\right)^{\frac{1}{2\gamma}(\alpha+\beta\eta)}\right] \tag{29}$$

4.3. Parameter analysis and validation of the statistical damage constitutive model

4.3.1. Parameter analysis of the statistical damage constitutive model for thermal insulation materials

Based on the established statistical damage constitutive model for HGM/EP materials, the analysis focuses on analyzing the influence of the dissipated energy weight factor η, the stiffness degradation factor γ, and the weighting coefficients (α, β) on the damage variable D of the material. Analysis of the composite properties reveals a significant positive correlation between η and γ ($\eta\propto\gamma$). Therefore, η is used to represent their coupled variation during parameter analysis, while α represents the variation in the weighting coefficients. As shown in Fig. 6, the damage variable D of HGM/EP materials exhibits an inverted L-shaped growth trend with increasing cell strength χ, where the damage variation rate ($\mathrm{d}D/\mathrm{d}\chi$) initially increases and then decreases. When D rapidly increases to approximately 0.9, it enters an inflection point, after which it slowly approaches 1.

Further analysis of the steep growth phase of the damage variable D reveals that, as the dissipated energy weight factor η increases from 0.6 to 1.4, the damage variation rate of the HGM/EP material consistently increases. Moreover, the variation of this rate with the weighting coefficient α exhibits two distinct regimes depending on the value of η. Taking $\eta=1$ as a threshold, the damage variation rate becomes insensitive to α. In other cases, there exists a cell strength threshold χ, which increases with increasing η, as indicated by the points connected by arrow ⑤ in Fig. 6. When $\eta<1$, the damage variation rate exhibits a clockwise pattern: it first rises and then declines with increasing α around the corresponding χ. Conversely, when $\eta>1$, a counterclockwise pattern is observed: the rate first declines and then rises with increasing α around the corresponding damage variation rate transition point χ.

According to the above parameter analysis results, the dissipated energy weight factor η, stiffness degradation factor γ, and weighting coefficients (α, β) all have significant impacts on the evolution of the damage variable D, thereby influencing the stress–strain characteristics of HGM/EP materials. Specifically, the uniaxial compressive mechanical behavior of HGM/EP materials at different temperature and pressure pretreatments determines the values of η and γ. When $\eta=1$, the damage variable D is unaffected by the weighting coefficients. For cases where

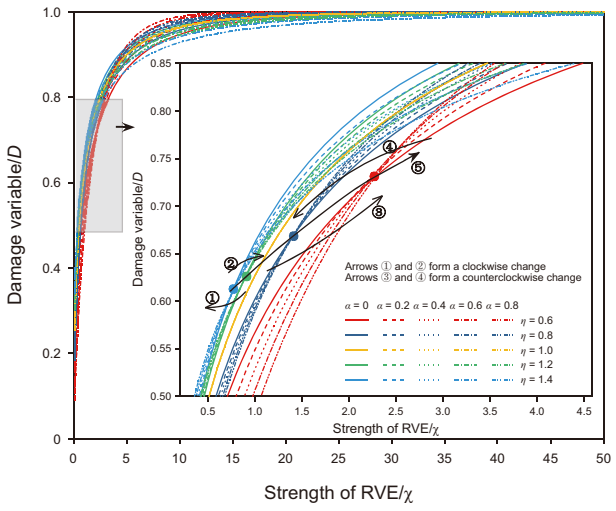

Fig. 6. Curves of the damage variable D versus cell strength χ for HGM/EP materials under different dissipated energy weight factors η and weighting coefficients α.

Table 1
Weighting coefficients of the statistical damage constitutive model for HGM/EP materials under various temperature–pressure conditions.

Pretreatment environment		K46-f40		K46-f50	
		α	β	α	β
H0	T25	0.4	0.6	0.2	0.8
	T50	0.3	0.7	0.2	0.8
	T100	0.4	0.6	0.35	0.65
	T150	0.5	0.5	0.5	0.5
H50	T25	0.4	0.6	0.35	0.65
	T50	0.5	0.5	0.25	0.75
	T100	0.5	0.5	0.6	0.4
	T150	0.5	0.5	0.5	0.5
H100	T25	0.45	0.55	0.3	0.7
	T50	0.45	0.55	0.25	0.75
	T100	0.5	0.5	0.5	0.5
	T150	0.4	0.6	0.45	0.55
H140	T25	0.55	0.45	0.25	0.75
	T50	0.55	0.45	0.8	0.2
	T100	0.5	0.5	0.5	0.5
	T150	0.5	0.5	0.5	0.5

η= 0.8 or η= 1.2, the stress–strain responses under different weighting coefficients were further analyzed, as shown in Fig. 7.

Changes in weighting coefficients α do not influence the nearly linear-elastic stage prior to the peak, but significantly affect the peak strength and post-peak stress drop characteristics. When η= 0.8, the peak strength decreases and the post-peak stress drop rate increases with increasing α; conversely, when η= 1.2, the peak strength rises and the post-peak stress decline rate decreases with increasing α. Therefore, accurately predicting the mechanical response of insulation materials after various temperature and pressure pretreatments relies on selecting appropriate weighting coefficients.

4.3.2. Verification of the statistical damage constitutive model for thermal insulation materials

To validate the statistical damage constitutive model for HGM/EP materials, it is first needed to determine the weighting coefficients α and β under different temperature–pressure pretreatment conditions. These coefficients can be obtained through fitting based on partial experimental data, as shown in Table 1.

Based on the obtained weighting coefficients, theoretical stress–strain responses for the HGM/EP composite were calculated by substituting them into the statistical damage constitutive model in Eq. (29). A comparison between the theoretical predictions and experimental results is shown in Fig. 8.

Comparison of the theoretical prediction results with the experimental results shows that the statistical damage constitutive model developed by introducing the dissipated energy scaling factor η, the stiffness degradation factor γ, and the weighting coefficients (α, β) exhibits improved predictive accuracy. This confirms that the influence of temperature and pressure pretreatment of HGM/EP materials can be effectively evaluated using η and γ, while the compressive strength and failure characteristics are accurately captured by the weighting coefficients α and β. Furthermore, based on the parameter analysis results, in

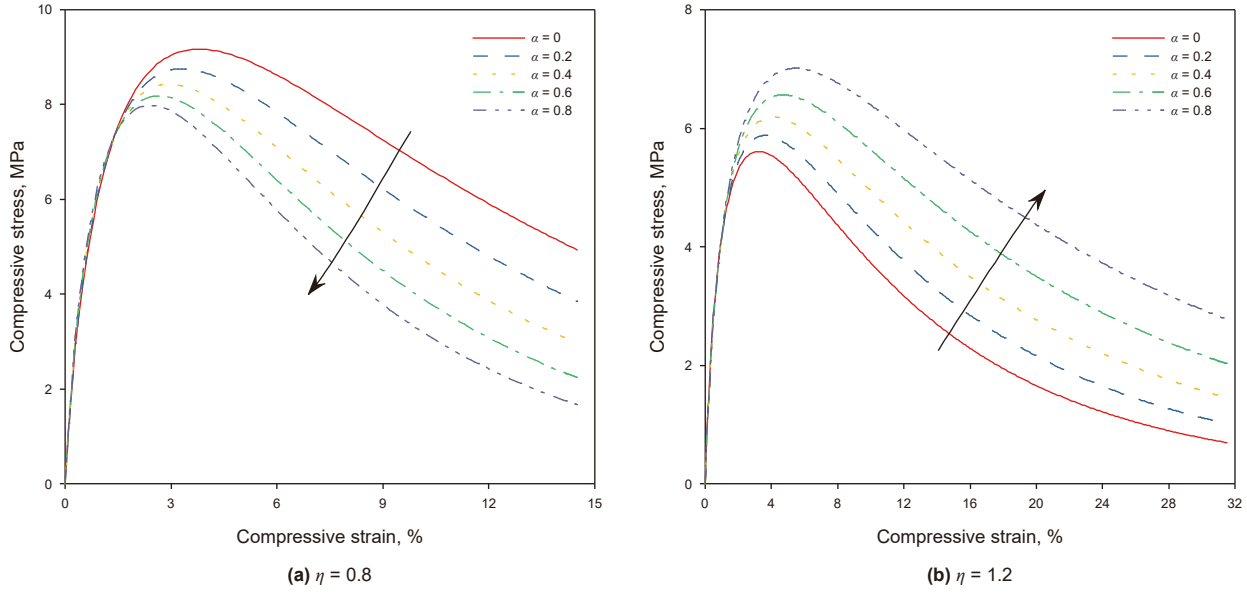

Fig. 7. Theoretical stress–strain curves of HGM/EP materials under different weighting coefficients α.

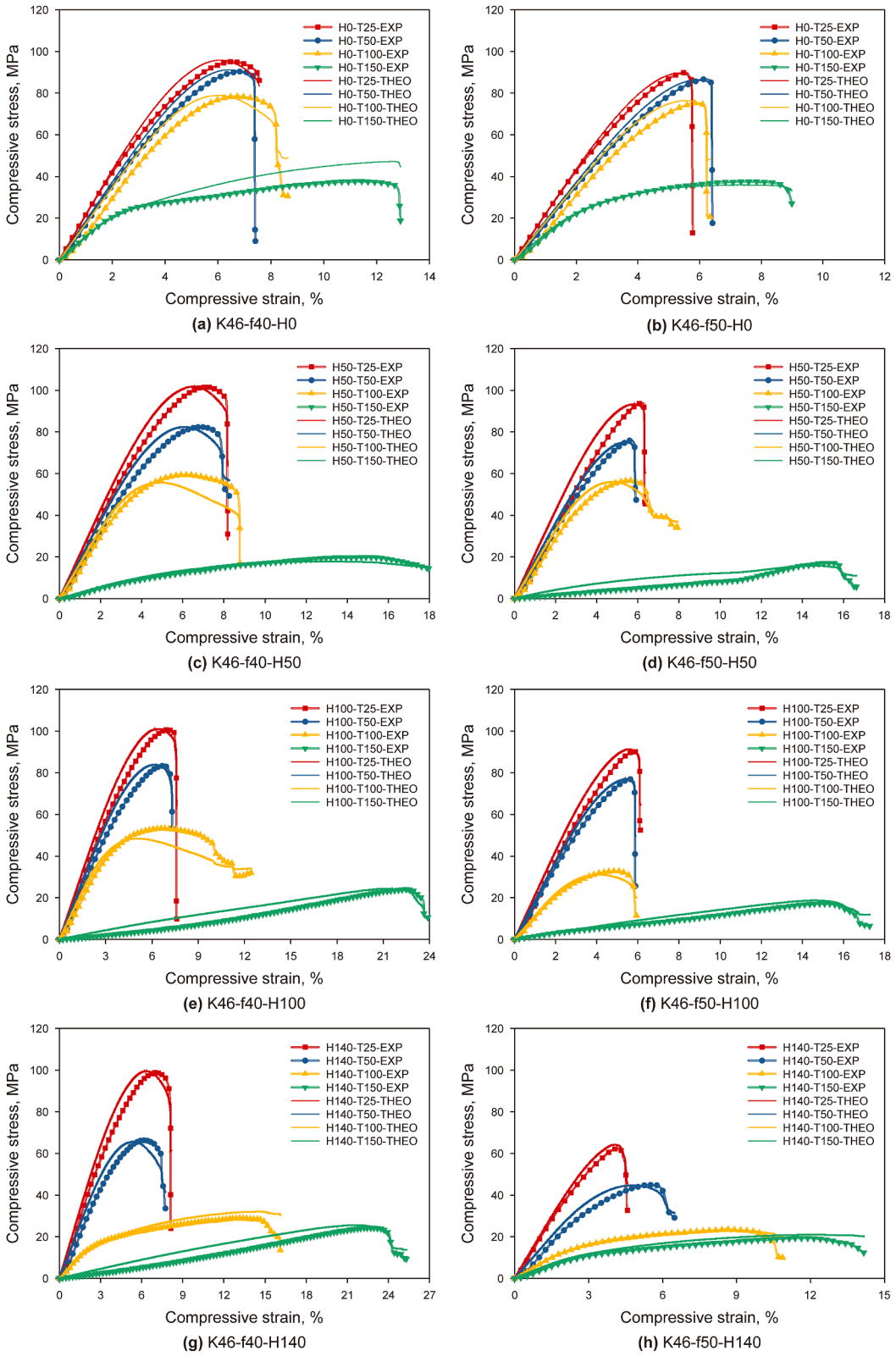

Fig. 8. Predicted values from the statistical damage constitutive model and experimental stress–strain curves of HGM/EP materials at different temperature and pressure situations.

order to reduce the damage accumulation rate of insulation materials under HTHP conditions, it is recommended to minimize η and γ. This can be achieved in future insulation material optimization by enhancing microsphere strength, improving interfacial bonding, and increasing the thermal resistance of the matrix.

5. Correlation between cell strength of thermal insulation materials and temperature–pressure conditions

To further analyze the initial damage induced by temperature–pressure pretreatment and the damage evolution behavior of HGM/EP materials during uniaxial compression, the variation of the cell strength χ in the statistical damage constitutive model with respect to compressive strain ε was examined. The variation patterns under different pretreatment conditions were similar; therefore, the condition of 140 MPa and 150 °C is taken as a representative example. As illustrated in Fig. 9, the cell strength χ increases nonlinearly with compressive strain, which can be approximated by a cubic function. Thus, the relationship between cell strength χ and compressive strain ε is expressed as Eq. (29):

$$\chi = A\varepsilon^3 + d \tag{30}$$

In this equation, d represents the initial damage induced in the HGM/EP material by the temperature-pressure pretreatment, while A reflects the damage rate during the pre-peak stage of uniaxial compression.

The fitting effect of the constructed functional relationship is satisfactory, with R^2 values greater than 0.95. Further analysis of the temperature and pressure dependence of the initial damage (d) and damage rate (A) provides a basis for the effective use of HGM/EP materials in HTHP extreme environments.

5.1. Initial damage evolution model considering temperature and pressure effects

During the HTHP pretreatment stage, the penetration of HTHP fluids causes the rupture of HGMs, interface damage, and water absorption at weak points in the HGM/EP materials, resulting in initial damage. To quantitatively analyze the initial damage, the initial damage parameter (d) is obtained from the relationship between the cellular strength (χ) and compressive strain ε. The value of d under standard temperature and pressure is defined as the reference value d^*. The initial damage values (d) under other conditions are then compared with the reference value d^* to obtain the relative initial damage d'.

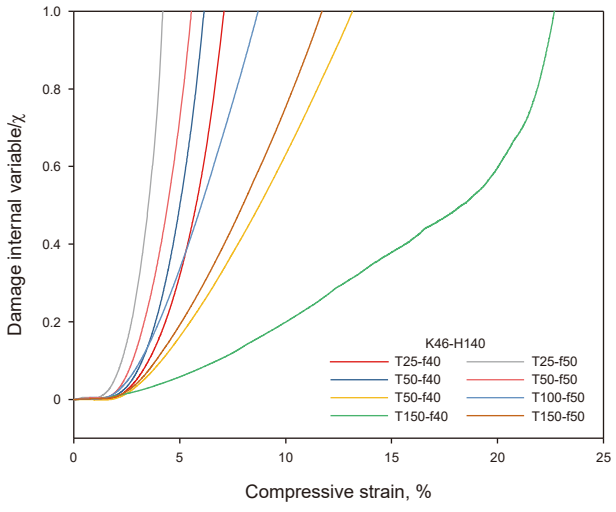

Fig. 9. Variation curve of the cellular strength χ of HGM/EP materials with compressive strain ε under 140 MPa conditions.

$$d' = d - d^* \tag{31}$$

Fig. 10 presents the relative initial damage d' of HGM/EP materials under different coupled temperature-pressure environments d'. When the pressure does not exceed 100 MPa, the relative initial damage shows a two-stage variation with temperature: it increases slowly below 100 °C but rises sharply at 150 °C. However, at a pressure of 140 MPa, the relative initial damage increases linearly with temperature. This is due to the weak interface formed between the HGMs and the matrix in the HGM/EP material, which is infiltrated by HTHP water, causing the HGMs to fracture (Wei et al., 2025). The cavities formed are then filled with HTHP water, which is the primary reason of the initial damage. This is consistent with the test results showing that the water absorption rate of HGM/EP materials increases with the rise in temperature and pressure (as discussed in Section 3.1).

Furthermore, to analyze the contribution of temperature and pressure to the formation of initial damage in HGM/EP materials, an evolution model for initial damage incorporating these effects is proposed, as expressed in the following equation:

$$d' = \xi T_{\mathrm{norm}}^{\psi} + \omega P_{\mathrm{norm}}^{\delta} + \kappa (T_{\mathrm{norm}} P_{\mathrm{norm}})^{\nu} \tag{32}$$

$$T_{\mathrm{norm}} = \frac{T - 25}{150 - 25}, P_{\mathrm{norm}} = \frac{P}{140} \tag{33}$$

In this equation, the terms $\xi T_{\mathrm{norm}}^{\psi}$, $\omega P_{\mathrm{norm}}^{\delta}$ and $\kappa (T_{\mathrm{norm}} P_{\mathrm{norm}})^{\nu}$ represent the initial damage caused to the HGM/EP materials by pure temperature, pure pressure, or temperature-pressure coupling pretreatment, respectively.

Because the relative initial damage d' increases exponentially with temperature at pretreatment pressures ≤100 MPa but linearly at 140 MPa, the analysis is conducted in two stages. First, the effects of temperature and pressure on initial damage are analyzed for pressures below 100 MPa. Subsequently, further analysis is performed based on the distinct linear damage characteristics observed at 140 MPa.

For pretreatment pressures below 100 MPa, the parameters describing the variation of relative initial damage d' with temperature and pressure variation are shown in Table 2. The coefficient of the temperature term (ξ) is notably larger than those of the pressure term (ω) and the temperature-pressure coupling term (γ and κ), This indicates that the initial damage of HGM/EP materials is dominated by the thermal effect, followed by the coupled temperature-pressure effect, with the influence of pure pressure being relatively minor.

However, extending Eq. (32) to fit the initial damage of HGM/EP materials under 140 MPa using the parameters in Table 2 results in slight deviations, as shown in Fig. 11. This is because, at 140 MPa, the relative initial damage increases linearly rather than exponentially with temperature. Therefore, the temperature-pressure coupling evolution model of initial damage based on Eq. (32) is modified as follows:

$$d' = \xi T_{\mathrm{norm}} + \omega \tag{34}$$

Therefore, while the pretreatment pressure is 140 MPa, the parameters in Eq. (34) are listed in the table below. Compared with Table 3, it can be noted that the value of ω remains constant, while the value of ξ increases This indicates that the contribution of pressure to the initial damage remains constant, while the thermal influence becomes more pronounced. Consequently, the evolution of initial damage in the HGM/EP materials under 140 MPa transitions to a linear increase.

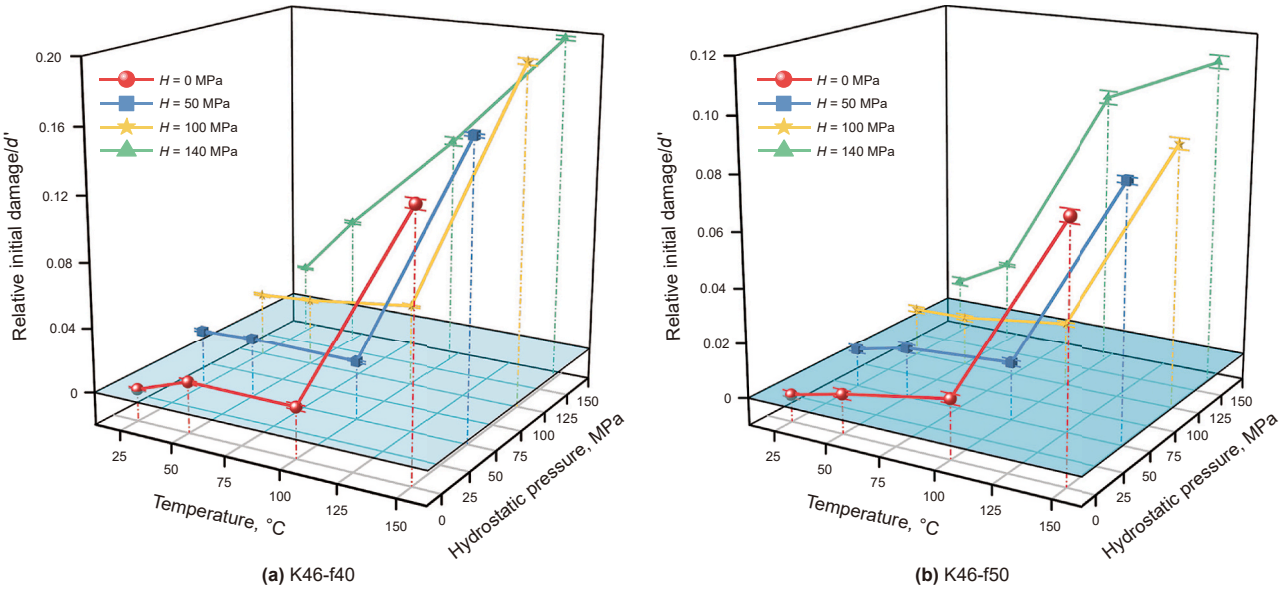

Fig. 10. Variation curve of relative initial damage d' of HGM/EP materials with temperature and pressure.

Table 2
Model parameters of the initial damage evolution model considering temperature and pressure effects under pressures below 100 MPa.

Material	ξ	Ψ	ω	δ	κ	ν	R^2
K46-f40	0.14	6.35	0.026	0.49	0.087	3.26	0.99
K46-f50	0.079	4.36	0.0098	0.62	0.042	3.98	0.97

5.2. Correlation of damage rate (A) with temperature, pressure, and initial damage

Furthermore, the damage rate A is obtained from the relationship between the cellular strength χ and compressive strain of HGM/EP materials. This parameter is used to analyze the damage evolution during uniaxial compression following various temperature-pressure pretreatments. A smaller A value indicates a slower damage progression.

Fig. 12 illustrates that the damage rate parameter A under different pressure treatments decreases continuously with increasing temperature, exhibiting a two-stage pattern. Below 100 °C, A decreases gradually, whereas at 150 °C, it declines rapidly. For the K46-f40 material, the damage rate A begins to decrease significantly from 50 °C under 140 MPa pressure, whereas for the K46-f50 material, A continues to decrease with increasing temperature. This observation contrasts with the conventional expectation that elevated temperature accelerates damage by enhancing molecular mobility or reducing the viscoelastic modulus. Instead, it is closely related to the variation characteristics of the relative initial damage d' and water absorption rate. Following HTHP pretreatment, the relatively weak regions within the HGM/EP materials have already been damaged, leaving behind regions with higher material strength.

The relationship between the damage rate A, the ambient test temperature T, and the relative initial damage d' is further analyzed

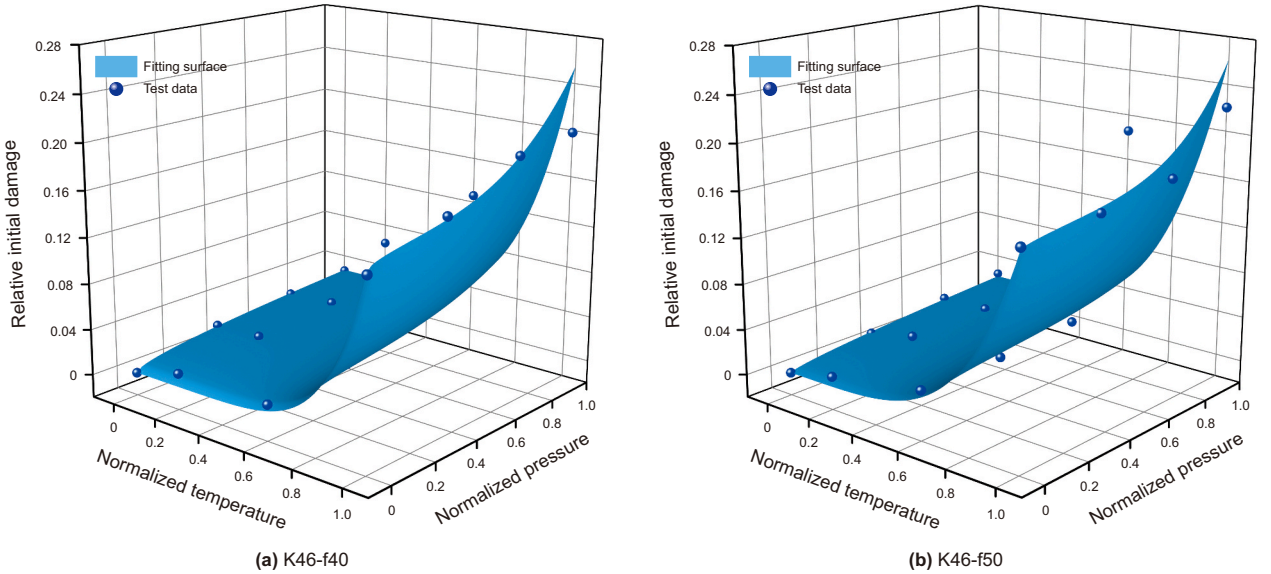

Fig. 11. Predictive performance of the temperature-pressure coupling evolution model for initial damage in HGM/EP materials.

Table 3
Model parameters of the initial damage evolution model considering temperature and pressure effects under 140 MPa pressure.

Material	ξ	ω	R^2
K46	0.17	0.026	0.99
K46	0.11	0.0098	0.99

in Fig. 13. Although rising test temperature increases the mobility of molecular chain segments during loading, the damage-promoting effect of this thermal activation competes with the damage-inhibiting effect arising from the initial damage state. As the pretreatment temperature and pressure increase, the damage-enhancing effect of matrix thermal activation becomes progressively weaker than the damage-suppressing effect caused by initial damage. Consequently, the damage rate of the material decreases continuously and gradually approaches zero.

In summary, after HTHP coupling pretreatment, the initial damage of HGM/EP materials continuously rises with both pretreatment temperature and pressure. However, the damage rate under uniaxial compression decreases continuously. The opposite trends of these two factors are due to the damage and failure of the material weak part, such as the microspheres and interfaces, during the pretreatment stage, which results in a defect shielding

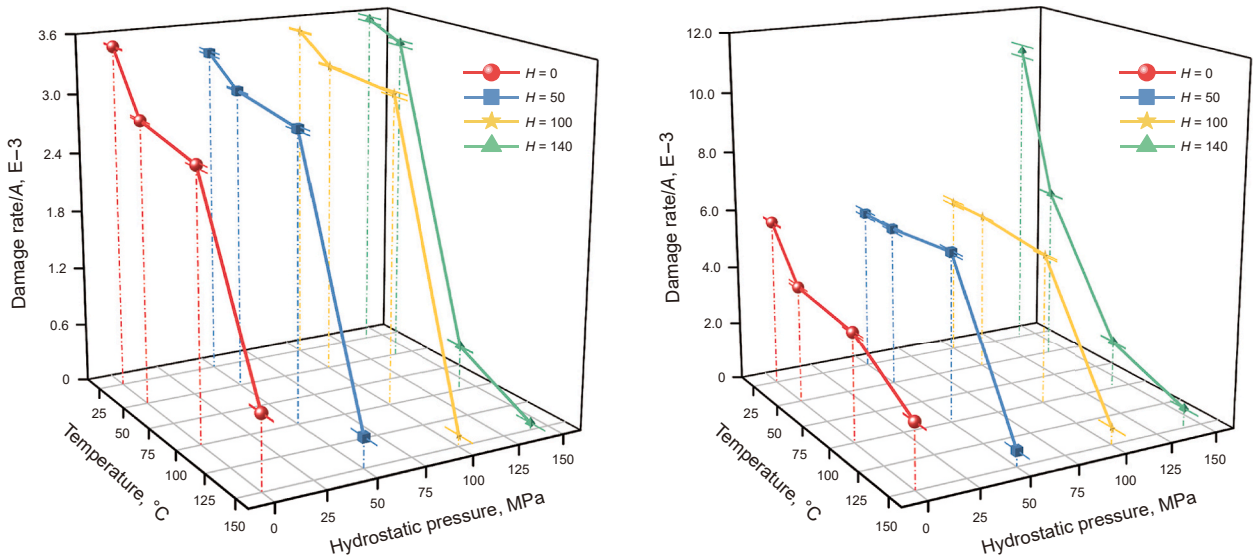

(a) K46-f40 **(b)** K46-f50

Fig. 12. Variation curves of damage rate of HGM/EP materials with temperature and pressure.

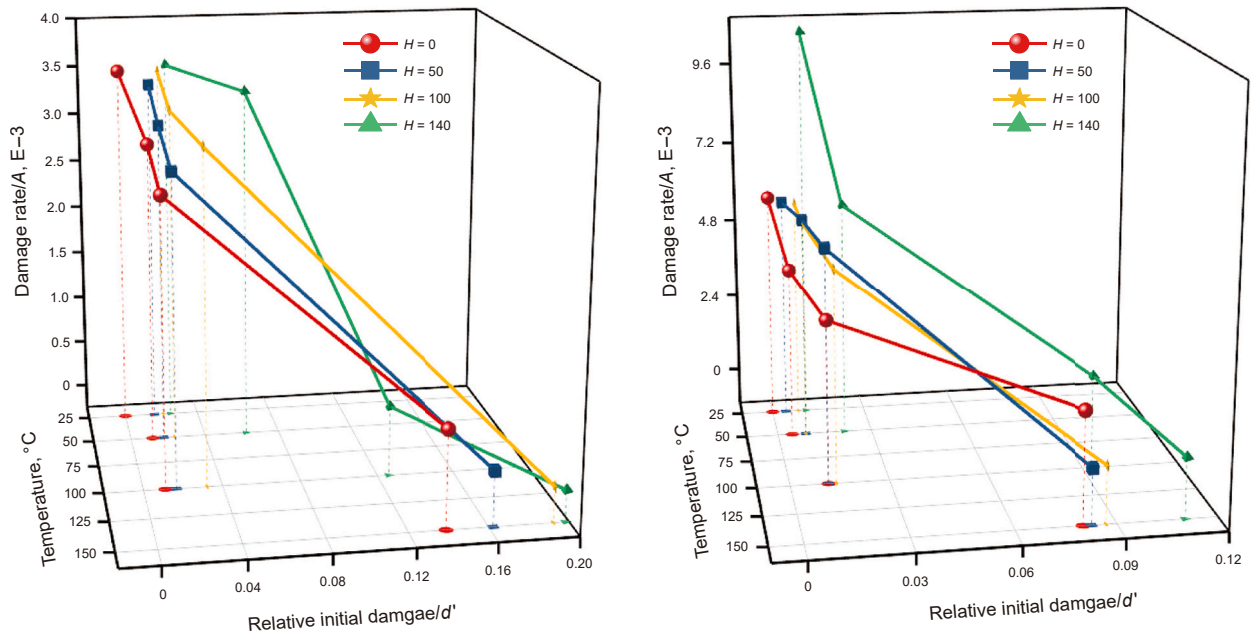

(a) K46-f40 **(b)** K46-f50

Fig. 13. Variation curves of damage rate of HGM/EP materials with loading temperature and initial damage.

effect. This shielding effect ultimately reduces the damage rate of the HGM/EP materials under uniaxial compression.

6. Conclusions

Regarding the performance changes of HGM/EP materials after temperature-pressure pretreatment, the variation laws of their physical and mechanical properties were analyzed. The energy evolution behavior during the uniaxial compression was explored, and a statistical damage constitutive model was established. The correlation between initial damage and damage rate with temperature and pressure were discussed. The main conclusions are as follows:

1. The variation rules of the properties of K46-f40 and K46-f50 HGM/EP materials after HTHP pretreatment were analyzed. High pressure is the primary factor leading to increased water absorption in the material. The infiltration of high-pressure water causes microsphere fracture, and the subsequent filling of the cavities establishes interconnected pathways for heat transfer, thereby enhancing thermal conductivity. Simultaneously, elevated temperature accelerates water infiltration and increases molecular chain mobility, further contributing to the rise in thermal conductivity. Furthermore, increasing pretreatment temperature softens the epoxy matrix, causing a transition from brittle to plastic failure and resulting in three characteristic types of stress-strain curves. High pressure facilitates this brittle-to-ductile transition.
2. Based on energy analysis, the damage evolution of HGM/EP materials during uniaxial compression after different temperature-pressure pretreatments was elucidated. When the pretreatment pressure does not exceed 50 MPa, the energy evolution is characterized by a transition at 100 °C from a regime dominated by elastic strain energy storage in the matrix to one governed by energy dissipation through matrix plastic deformation and microsphere damage. At elevated temperatures approaching the glass transition temperature, the epoxy matrix undergoes a progressive transition, leading to a deformation mechanism dominated by plastic flow. This is characterized by a continuous increase in energy dissipation.
3. A statistical damage constitutive model was developed for the HGM/EP composite. The model employs the dissipated energy weight factor (η) and the stiffness degradation factor (γ) to assess the effects of temperature-pressure pretreatment on mechanical properties. The introduced weighting coefficients (α, β) reveal that, as α increases, the variation in the damage evolution rate ($dD/d\chi$) with respect to a characteristic element strength follows one of two patterns: an initial increase followed by a decrease, or an initial decrease followed by an increase. The constructed model provides accurate predictions of the stress–strain response. The constructed initial damage evolution model indicates that the pre-treatment temperature is the key factor governing the accumulation of initial damage d, while the temperature-pressure coupling further exacerbates damage. Based on the integrated analysis of the physical-mechanical properties and damage evolution of both K46-f40 and K46-f50 thermal insulation materials, they are considered suitable for in-situ deep rock coring applications at temperatures up to 100 °C and pressures up to 100 MPa.

CRediT authorship contribution statement

Zi-Jie Wei: Writing – review & editing, Writing – original draft, Investigation, Data curation. **Zhi-Qiang He:** Writing – review & editing, Visualization, Supervision, Investigation, Funding acquisition, Data curation. **Ling Chen:** Investigation, Formal analysis, Data curation. **Bo Yu:** Investigation, Formal analysis, Data curation. **Jian-Ping Yang:** Investigation, Formal analysis, Data curation. **Hai-Shu Bai:** Investigation, Formal analysis, Data curation. **He-Ping Xie:** Supervision, Resources, Project administration, Methodology, Conceptualization.

Declaration of competing interest

The authors declare that they have no known competing financial interests or personal relationships that could have appeared to influence the work reported in this paper.

Acknowledgments

This work was supported by the National Natural Science Foundation of China (Grant No. 52304033), China Postdoctoral Science Foundation (Grant No. 2025T180116), Coal-Major Project (Grant No. 2025ZD1700902) and Ministry of Education of China (Grant No. JYB2025XDXM311).

References

Abedin, R., Feng, X., Pojman Jr., J., et al., 2022. A thermoset shape memory polymer-based syntactic foam with flame retardancy and 3D printability. ACS Appl. Polym. Mater. 4 (2), 1183–1195. https://doi.org/10.1021/acsapm.1c01596.

Bao, F., Wang, J., Wang, J., et al., 2020. Static and impact responses of syntactic foam composites reinforced by multi-walled carbon nanotubes. J. Mater. Res. Technol-JMRT 9 (6), 12391–12403. https://doi.org/10.1016/j.jmrt.2020.08.079.

Cao, S., Ma, N., Zhang, Y., et al., 2023. Fabrication, mechanical properties, and multifunctionalities of particle reinforced foams: A review. Thin-Walled Struct. 186, 110678. https://doi.org/10.1016/j.tws.2023.110678.

Chandra, D., Bakshi, T., Vishal, V., 2021. Thermal effect on pore characteristics of shale under inert and oxic environments: Insights on pore evolution. Microporous Mesoporous Mater. 316, 110969. https://doi.org/10.1016/j.micromeso.2021.110969.

Chen, Y., Wang, J., Wen, S., et al., 2021. Zinc phosphate coated modified hollow glass beads and their thermal insulation and anticorrosion performance in coatings. Ceram. Int. 47 (16), 23507–23517. https://doi.org/10.1016/j.ceramint.2021.05.067.

Deng, J.A., Cu, D.S., 2011. On a statistical damage constitutive model for rock materials. Comput. Geosci. 37 (2), 122–128. https://doi.org/10.1016/j.cageo.2010.05.018.

Doddamani, M., 2019. Effect of surface treatment on quasi-static compression and dynamic mechanical analysis of syntactic foams. Compos Pt B-Eng. 165, 365–378. https://doi.org/10.1016/j.compositesb.2019.01.076.

Garcia, C.D., Shahapurkar, K., Doddamani, M., et al., 2018. Effect of arctic environment on flexural behavior of fly ash cenosphere reinforced epoxy syntactic foams. Compos Pt B-Eng. 151, 265–273. https://doi.org/10.1016/j.compositesb.2018.06.035.

He, Z., Xie, H., Gao, M., et al., 2024a. In situ temperature-preserved coring for deep oil and gas reservoir: thermal insulation materials. J. Rock Mech. Geotech. Eng. 17 (9), 5601–5614. https://doi.org/10.1016/j.jrmge.2024.10.008.

He, Z.Q., Xie, H.P., Chen, L., et al., 2024b. Research on thermal insulation materials properties under HTHP conditions for deep oil and gas reservoir rock ITP-Coring. Pet. Sci. 21 (4), 2625–2637. https://doi.org/10.1016/j.petsci.2024.03.005.

He, Z.Q., Xie, H.P., Gao, M.Z., et al., 2020. Design and verification of a deep rock corer with retaining the in situ temperature. Adv. Civ. Eng. 2020 (1), 8894286. https://doi.org/10.1155/2020/8894286.

He, Z.Q., Yang, Y., Yu, B., et al., 2022. Research on properties of hollow glass microspheres/epoxy resin composites applied in deep rock in-situ temperature-preserved coring. Pet. Sci. 19 (2), 720–730. https://doi.org/10.1016/j.petsci.2021.10.028.

Huang, R.X., Li, P.F., 2015. Elastic behaviour and failure mechanism in epoxy syntactic foams: the effect of glass microballoon volume fractions. Compos Pt B-Eng. 78, 401–408. https://doi.org/10.1016/j.compositesb.2015.04.002.

Lemaitre, J., 1984. How to use damage mechanics. Nucl. Eng. Des. 80 (2), 233–245. https://doi.org/10.1016/0029-5493(84)90169-9.

Li, R., Xu, Y., Zhang, K.H., et al., 2024. A novel computational model based on molecular chain dynamics: Quantification and evaluation of interfacial interactions in polymer-based composite materials. Compos. Adv. Mater. 33, 1–12. https://doi.org/10.1177/26349833241309350.

Lin, T., Meng, W., Chen, Y.D., et al., 2023. Unloading-induced permeability recovery in rock fractures. J. Rock Mech. Geotech. Eng. 15 (12), 3148–3162. https://doi.org/10.1016/j.jrmge.2023.06.002.

Liu, G., 2019. Novel test method for the hydrostatic properties of syntactic foams. Results Mater. 1, 100010. https://doi.org/10.1016/j.rinma.2019.100010.
Liu, S.W., Lei, X., Feng, C.G., et al., 2016. Estimation of subsurface formation temperature in the Tarim Basin, northwest China: Implications for hydrocarbon generation and preservation. Int. J. Earth Sci. 105 (5), 1329–1351. https://doi.org/10.1007/s00531-015-1253-4.
Pei, L.Z., Ya, B., Huang, S.H., et al., 2025. Construction of multilevel interfacial structures and their effect on the properties of syntactic foams. Appl. Surf. Sci. 688, 162435. https://doi.org/10.1016/j.apsusc.2025.162435.
Phan, V.T., Choqueuse, D., Cognard, J.Y., et al., 2013. Experimental analysis and modelling of the long term thermo-mechanical behaviour of glass/polypropylene syntactic used on thermally insulated offshore pipeline. Prog. Org. Coating 76 (2–3), 341–350. https://doi.org/10.1016/j.porgcoat.2012.09.028.
Porfiri, M., Gupta, N., 2009. Effect of volume fraction and wall thickness on the elastic properties of hollow particle filled composites. Compos Pt B-Eng. 40 (2), 166–173. https://doi.org/10.1016/j.compositesb.2008.09.002.
Saif, T., Lin, Q., Bijeljic, B., et al., 2017. Microstructural imaging and characterization of oil shale before and after pyrolysis. Fuel 197, 562–574. https://doi.org/10.1016/j.fuel.2017.02.030.
Schumacher, G., Murray, C.M., Park, J., et al., 2024. Energy absorption behavior of elastomeric matrix composites reinforced with hollow glass microspheres. Aerospace 11 (12), 1012. https://doi.org/10.3390/aerospace11121012.
Shahapurkar, K., Garcia, C.D., Doddaman, M., et al., 2018. Compressive behavior of cenosphere/epoxy syntactic foams in arctic conditions. Compos Pt B-Eng. 135, 253–262. https://doi.org/10.1016/j.compositesb.2017.10.006.
Shi, X.J., Xie, H.P., Li, C., et al., 2025. Performance of a deep in situ pressure-preserving coring controller in a high-temperature and ultrahigh-pressure test system. J. Rock Mech. Geotech. Eng. 17 (2), 877–896. https://doi.org/10.1016/j.jrmge.2024.01.012.
Sue, R., Wang, Y.N., Cheng, Y., 2022. Research progress of syntactic foams used in solid buoyance material. J. Mater. Eng. 50 (6), 86–96. https://doi.org/10.11868/j.issn.1001-4381.2021.000566.
Sun, J.S., Liu, W., Wang, Q., et al., 2024. Challenges and development prospects of oil and gas drilling and completion in myriametric deep formation in China. Drill. Prod. Technol. 47 (2), 1–9. https://doi.org/10.3969/J.ISSN.1006-768X.2024.02.01.
Tong, Y.Q., Shi, Q.S., Liu, M.J., et al., 2021. Lightweight epoxy-based abradable seal coating with high bonding strength. J. Mater. Sci. Technol. 69, 129–137. https://doi.org/10.1016/j.jmst.2020.05.077.
Wang, J.Z., Cui, W.C., 2023. A cross-scale hygro-mechanical coupling model for hollow glass bead/resin composite materials. Int. J. Solid Struct. 264, 112104. https://doi.org/10.1016/j.ijsolstr.2023.112104.
Wei, Z., He, Z., Chen, L., et al., 2025. Properties of thermal insulation materials for deep oil and gas in situ temperature-preserved coring: A focus on interphase. J. Rock Mech. Geotech. Eng. 17 (12), 7691–7710. https://doi.org/10.1016/j.jrmge.2025.01.026.
Wei, Z.J., He, Z.Q., Yang, J.P., 2024. Analysis of core temperature variation and its influencing factors in deep rock in-situ temperature-preserved coring. Adv. Geo-Energy Res. 14 (3), 215–223. https://doi.org/10.46690/ager.2024.12.06.
Wei, Z.J., Li, C., Yu, B., et al., 2023. Study on heat transfer model theory and numerical simulation used in deep rock in-situ temperature-preserved coring. Therm. Sci. 27 (1B), 639–646. https://doi.org/10.2298/TSCI2301639W.
Wu, X., Gao, Y., Wang, Y., et al., 2021. Recent developments on epoxy-based syntactic foams for deep sea exploration. J. Mater. Sci. 56 (3), 2037–2076. https://doi.org/10.1007/s10853-020-05420-w.
Xiao, Y.M., Qiao, Y.F., He, M.C., et al., 2023. Strain rate effect of siltstone under triaxial compression and its interpretation from damage mechanics. Rock Mech. Rock Eng. 56 (12), 8643–8656. https://doi.org/10.1007/s00603-023-03528-4.
Xie, H.P., Gao, F., Ju, Y., 2015. Research and development of rock mechanics in deep ground engineering. Chin. J. Rock Mech. Eng. 34 (11), 2161–2178. https://doi.org/10.13722/j.cnki.jrme.2015.1369 (in Chinese).
Xie, H.P., Gao, M.Z., Zhang, R., et al., 2020. Study on concept and progress of in situ fidelity coring of deep rocks. Chin. J. Rock Mech. Eng. 39 (5), 865–876. https://doi.org/10.13722/j.cnki.jrme.2020.0138 (in Chinese).
Xie, H.P., Gao, M.Z., Zhang, R., et al., 2019. Study on the mechanical properties and mechanical response of coal mining at 1000m or deeper. Rock Mech. Rock Eng. 52 (5), 1475–1490. https://doi.org/10.1007/s00603-018-1509-y.
Xie, H.P., Hu, Y.Q., Gao, M.Z., et al., 2023. Research progress and application of deep in-situ condition preserved coring and testing. Int. J. Min. Sci. Technol. 33 (11), 1319–1337. https://doi.org/10.1016/j.ijmst.2023.06.007.
Xie, H.P., Ju, Y., Li, L.Y., 2005. Criteria for strength and structural failure of rocks based on energy dissipation and energy release principles. Chin. J. Rock Mech. Eng. (17), 3003–3010. https://doi.org/10.3321/j.issn:1000-6915.2005.17.001 (in Chinese).
Xie, H.P., Liu, T., Gao, M.Z., et al., 2021. Research on in-situ condition preserved coring and testing systems. Pet. Sci. 18 (6), 1840–1859. https://doi.org/10.1016/j.petsci.2021.11.003.
Xu, X.L., Karakus, M., 2018. A coupled thermo-mechanical damage model for granite. Int. J. Rock Mech. Min. Sci. 103, 195–204. https://doi.org/10.1016/j.ijrmms.2018.01.030.
Yang, J.P., Chen, L., Gu, X.B., et al., 2022. Hollow glass microspheres/silicone rubber composite materials toward materials for high performance deep in-situ temperature-preserved coring. Pet. Sci. 19 (1), 309–320. https://doi.org/10.1016/j.petsci.2021.11.012.
Zhai, G.J., Ding, Y., Ma, Z., et al., 2022. Novel triaxial experimental investigation on compressive behavior of hollow glass microspheres composites under varied temperature environments. Polym. Test. 115, 107745. https://doi.org/10.1016/j.polymertesting.2022.107745.
Zhai, G.J., Ding, Y., Wang, Y., et al., 2020. Experimental investigation of the hydrostatic compression of a hollow glass microspheres/epoxy resin under high-pressure conditions at the full ocean depth. Polym. Compos. 41 (12), 5331–5342. https://doi.org/10.1002/pc.25797.
Zhai, G.J., Wei, Z.H., Ma, Z., et al., 2023. Establishment and program development of failure criterion of hollow glass microspheres/epoxy resin composites based on tension/compression discrepancy. Eng. Fail. Anal. 149, 107270. https://doi.org/10.1016/j.engfailanal.2023.107270.
Zhang, L.H., Townsend, D., Petrinic, N., et al., 2022. The dependency of compressive response of epoxy syntactic foam on the strain rate and temperature under rigid confinement. Compos. Struct. 280, 114853. https://doi.org/10.1016/j.compstruct.2021.114853.
Zhang, X., Wang, P.P., Zhou, Y.H., et al., 2016. The effect of strain rate and filler volume fraction on the mechanical properties of hollow glass microsphere modified polymer. Compos Pt B-Eng. 101, 53–63. https://doi.org/10.1016/j.compositesb.2016.06.079.